Modeling heat transfer in supercritical fluid using the lattice Boltzmann method

Gábor Házi* and Attila Márkus
Simulator Development Department, KFKI Atomic Energy Research Institute, H-1525 Budapest, Hungary
(Received 3 October 2006; revised manuscript received 26 November 2007; published 21 February 2008)

A lattice Boltzmann model has been developed to simulate heat transfer in supercritical fluids. A supercritical viscous fluid layer between two plates heated from the bottom has been studied. It is demonstrated that the model can be used to study heat transfer near the critical point where the so-called piston effect speeds up the transfer of heat and results in homogeneous heating in the bulk of the layer. We have also studied the onset of convection in a Rayleigh-Bénard configuration. It is shown that our model can well predict qualitatively the onset of convection near the critical point, where there is a crossover between the Rayleigh and Schwarzschild criteria.

DOI: 10.1103/PhysRevE.77.026305 PACS number(s): 47.40.−x, 47.55.pb, 47.11.Qr, 02.70.−c

I. INTRODUCTION

As the industrial importance of supercritical fluids has been increasing rapidly, a better understanding of transport phenomena around and above the critical point is desired. A fluid is in a supercritical state when its temperature and pressure exceed their critical points (T_c, p_c). As the critical point is approached, several thermophysical properties of the fluid show strong divergence; for example the isothermal compressibility and isobaric thermal expansion tend to infinity, while the thermal diffusivity tends to zero [1]. Due to these specific material properties, a new adiabatic process, often called the ''piston effect'' [2,3], can play an important role in heat transfer problems near the critical point.

Basically, this effect can be explained as follows. When the wall of a cell filled with a near-critical fluid is heated, a thin thermal boundary layer forms at the wall. Due to the high expansion coefficient of the fluid, the layer can expand very rapidly and, like a piston, it can compress the rest of the highly compressible fluid. The compression results in a homogeneous temperature rise in the fluid [3]. In a microgravity environment it was demonstrated that the heat transfer speeds up due to this mechanism [4], instead of the critical slowing down scenario, which had been expected because of the low thermal diffusivity near the critical point [5,6].

It is worth noting that the material properties also change abruptly far above the critical pressure, around the pseudocritical temperature, where, e.g., the specific heat increases rapidly. Accordingly we expect anomalous heat transfer in this range of parameters, too. This expectation is supported by several observations obtained in large-scale experimental facilities in terrestrial conditions [7].

In the last decade a number of numerical computations based on the finite-volume approach have been reported studying various aspects of heat transfer near the critical point [8–13].

In this paper, we propose a numerical approach to study heat transfer in supercritical fluid. Our approach is based on the lattice Boltzmann method, which has recently achieved considerable success in simulating various transport phenomena.

The rest of the paper is organized as follows. In Sec. II the governing equations for the supercritical fluid are briefly discussed. In Sec. III the proposed lattice Boltzmann model is introduced. Section IV presents numerical simulations of classical heat transfer problems of supercritical fluids. The adiabatic heating of the fluid by the piston effect is demonstrated by simulating heat transfer in a supercritical fluid layer near the critical point. As a second example, the Rayleigh-Bénard convection is studied at various thermal expansion coefficients. It is shown that the simulations give qualitative agreement with theoretical results and other numerical calculations.

II. GOVERNING EQUATIONS FOR SUPERCRITICAL FLUID

Although major characteristics of heat transfer near the critical point can be studied by simple model equations, the compressible Navier-Stokes equations supplemented by a proper form of the energy equation provide a firm foundation for a complete description of the phenomena. Accordingly, the following set of macroscopic equations are approximated in our approach:

$$\partial_t \rho + \partial_\alpha(\rho u_\alpha) = 0 \tag{1}$$

$$\partial_t(\rho u_\alpha) + \partial_\beta(\rho u_\alpha u_\beta) = -\partial_\alpha p + \mu \partial_\beta S_{\alpha\beta} \tag{2}$$

$$\partial_t T + \partial_\alpha(T u_\alpha) = \partial_\alpha(D_{T,v}\partial_\alpha T) - \frac{T}{\rho c_v}(\partial_T p)_\rho \partial_\alpha u_\alpha, \tag{3}$$

where ρ, u, p, T, S, c_v, and μ are the density, velocity, pressure, temperature, strain rate, specific heat at constant volume, and dynamic viscosity, respectively. The symbol ∂_α denotes the derivative ∂/∂_α so, for instance, $(\partial_T p)_\rho = (\partial p/\partial T)_\rho$ is the thermodynamic tension. Following Einstein's convention, repeated indices imply summation. It became evident from the asymptotic analysis presented in [3] that the compression work plays a prominent role in the heat transfer problems we investigate here. Therefore, for simplicity, the heat due to friction was neglected in this work. Note also that the thermal diffusivity is defined at constant volume by

*gah@sunserv.kfki.hu

$$D_{T,v} \equiv \frac{k}{\rho c_v}, \tag{4}$$

where k is the heat conductivity.

The equation system above is closed by an equation of state. With a few exceptions (see, e.g., [14]), the van der Waals equation

$$p = \frac{\rho RT}{1 - b\rho} - a\rho^2 \tag{5}$$

or the linearized equation of state

$$\rho = \rho_0[1 + \kappa_T(p - p_0) - \alpha_p(T - T_0)] \tag{6}$$

is used for the simulation of supercritical fluids. In Eq. (5) R, a, and b are the universal gas and the van der Waals constants, respectively. In Eq. (6) ρ_0, p_0, and T_0 are reference values, $\kappa_T = (\partial\rho/\partial p)_T$ is the isothermal compressibility, and $\alpha_p = (\partial\rho/\partial T)_p$ is the isobaric thermal expansion coefficient.

Although these equation of states do not lead to accurate critical exponents, they proved to be useful in the understanding of the basic heat transfer mechanisms in supercritical fluids [3]. It is worth noting that, instead of solving Eqs. (1)–(3) directly, the acoustically filtered equations [15] are solved in most numerical studies. The filtering is equivalent to apply a low-Mach-number approximation. The basic outcome of acoustically filtered equations is that the pressure is composed of a spatially independent background part and an asymptotically smaller dynamical part:

$$p = p_0(t) + \mathrm{Ma}^2\, p^{(1)}(\mathbf{x},t) + o(\mathrm{Ma}^2), \tag{7}$$

where Ma is the Mach number and $p^{(1)}$ replaces p in the momentum equation after substitution and ordering; furthermore the equation of state is written as

$$\rho = \rho(T, p_0). \tag{8}$$

Hence the dynamical fluctuations in pressure do not enter into the equation of state. Note that an additional equation is needed for the assessment of p_0. In our approach, we will not use acoustic filtering; therefore we can represent the acoustics accurately. However, as we shall see, the relevant time scale (piston effect time scale) for the heat transfer in a supercritical fluid is much higher than the acoustic time scale, so the strict time step limit arising from the resolution of acoustic waves can be relaxed.

Note that, following Nikolayev *et al.* [14], we shall approximate Eq. (3), which is the "c_v formalism" of the energy equation. This formalism is preferred to the "c_p formalism," because of the much weaker divergence of c_v compared to c_p (specific heat at constant pressure) near the critical point. Indeed, expressing the specific heats in terms of $\varepsilon = T - T_c$, one can write $c_p \sim \varepsilon^{-1.2}$ [16] and $c_v \sim \varepsilon^{-0.1}$ [14]. Obviously, the divergence of c_v is less strong than that of c_p. This statement holds for a supercritical state around the pseudocritical temperature, too. As an example, Fig. 1 shows the specific heats of water at 220 bar around the pseudocritical temperature [17]. It is also worth noting that the thermal diffusivity defined by (4) remains almost constant below the pseudocritical temperature, while in the case of the c_p formalism

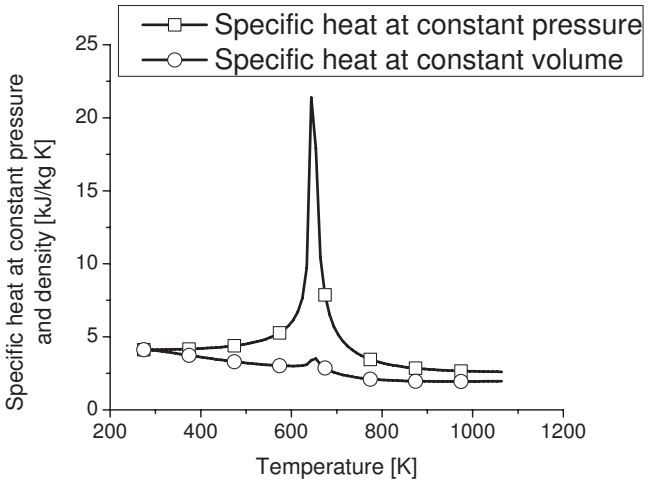

FIG. 1. Specific heats of water as a function of temperature at supercritical pressure.

$k/\rho c_p$ decreases rapidly in the same temperature range (Fig. 2). Nevertheless, we note that it is straightforward to modify our proposed model in conformity with the c_p formalism.

For treating buoyantly driven flows we use the Boussinesq approximation in line with some numerical studies of supercritical fluid (see, e.g., [13]). The principal assumption is that the density variation is small in the fluid, i.e., $\rho'/\rho \ll 1$. Note that this approximation restricts the scale height for motions such that, if L is the characteristic dimension for the motion, the hydrostatic density variation must remain small over this scale. The momentum equation is simplified by subtracting off the hydrostatic contribution and absorbing it into the pressure. Under the assumption that to leading order $\rho' = -\beta T'$, i.e., the dynamic pressure fluctuations cannot compete with temperature fluctuations in modifying density, the momentum equation can be written as follows:

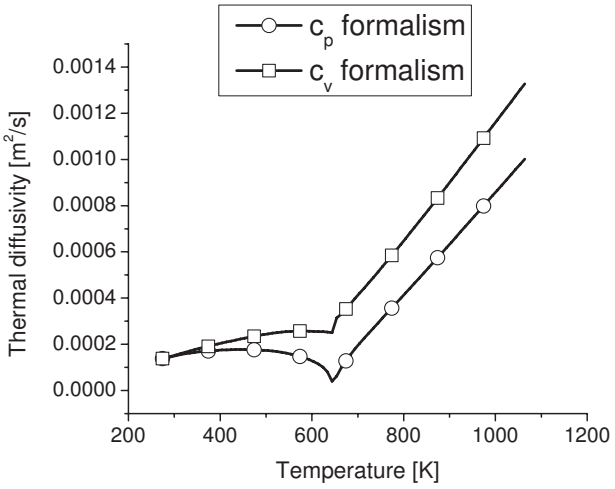

FIG. 2. Thermal diffusivity of water at constant volume and pressure as a function of temperature at supercritical pressure.

$$\partial_t u_\alpha + \partial_\beta (u_\alpha u_\beta) = -\frac{1}{\rho_0}\partial_\alpha p' - \alpha_p T g e_z + \frac{\mu}{\rho_0}\partial_\beta S_{\alpha\beta}. \quad (9)$$

It is worth mentioning that according to acoustic filtering ρ' corresponds to $\rho^{(1)}$ in the momentum equation. Finally we note that, following [18], the divergence of the thermal conductivity near the critical point can be taken into account by the following relation:

$$k = 1 + 0.75[(T - T_c)/T_c]^{-0.5}. \quad (10)$$

III. THE LATTICE BOLTZMANN METHOD

We use the lattice Boltzmann method [19–21] for the solutions of Eqs. (1), (3), and (9).

A. The continuity and momentum equations

For the solution of the Navier-Stokes equations with a nonideal gas equation of state, one can adopt the method of Shan and Chen [22]. For completeness we briefly recall the basic steps of this method.

The lattice Boltzmann equation using the Bhatnagar-Gross-Krook (BGK) [23,24] collision operator is given by

$$f_i(\mathbf{r} + c_{i\alpha}\delta t, t + \delta t) - f_i(\mathbf{r}, t) = -\frac{1}{\tau}[f_i(\mathbf{r}, t) - f_i^{\mathrm{eq}}(\mathbf{r}, t)], \quad (11)$$

where $f_i(\mathbf{r},t)$ is the one-particle velocity distribution function, $\mathbf{e}_i$ is the lattice velocity vector, τ is the relaxation time, which controls the rate of approach to the local equilibrium $f_i^{\mathrm{eq}}(\mathbf{r},t)$, and δt is the time step. For a two-dimensional nine-velocity (D2Q9) model the lattice vectors take the form $\mathbf{e}_i=[\cos(\pi\frac{i-1}{2}),\sin(\pi\frac{i-1}{2})]$, $i=1,2,3,4$, and $\mathbf{e}_i=\sqrt{2}[\cos(\pi\frac{i-9/2}{2}),\sin(\pi\frac{i-9/2}{2})]$, $i=5,6,7,8$, and the local equilibrium distribution function can be given by

$$f_i^{\mathrm{eq}} = w_i\rho\left(1 + \frac{1}{c_s^2}c_{i\alpha}u_\alpha^{\mathrm{eq}} + \frac{u_\alpha^{\mathrm{eq}}u_\beta^{\mathrm{eq}}}{2c_s^4}(c_{i\alpha}c_{i\beta} - c_s^2\delta_{\alpha\beta})\right), \quad (12)$$

where $u_\alpha^{\mathrm{eq}}=u_\alpha^*+a_\alpha\tau$ and $a_\alpha=F_\alpha/\rho$ represents the acceleration due to the intermolecular force F_α between molecules. u_α^* is calculated by taking the following moment of the distribution functions: $\rho u_\alpha^*=\Sigma_i f_i c_{i\alpha}$.

The lattice weights are given as follows: $w_0=\frac{4}{9}$, $w_i=\frac{1}{9}$ for $i=1,2,3,4$ and $w_i=\frac{1}{36}$ for $i=5,6,7,8$, and the lattice speed of sound is defined by $c_s^2=1/3$. The macroscopic quantities, density and hydrodynamic velocity, are calculated as follows:

$$\rho = \sum_i f_i, \quad u_\alpha = u_\alpha^* + \frac{1}{2}F_\alpha. \quad (13)$$

The intermolecular force is computed as the gradient of a suitable chosen interaction pseudopotential $\psi(\mathbf{r})$,

$$F_\alpha(\mathbf{r}) = -G\delta t\psi(\mathbf{r})\nabla\psi(\mathbf{r}), \quad (14)$$

where the parameter G controls the strength of the interaction. Using the lattice vectors the gradient can be approximated as follows:

$$\nabla\psi(\mathbf{r}) \simeq \frac{1}{\delta t}\sum_i q_i\psi(\mathbf{r} + \mathbf{c}_i)\mathbf{c}_i, \quad (15)$$

where $q_i=1/3$ for $i=1,2,3,4$ and $q_i=1/12$ for $i=5,6,7,8$.

Using this approximation, the force can be rewritten as

$$F_\alpha(\mathbf{r}) = \frac{G}{3}\psi(\mathbf{r})\sum_i q_i\psi(\mathbf{r} + c_{i\alpha})c_{i\alpha}. \quad (16)$$

In order to simulate van der Waals gases (5) the pseudopotential $\psi(\mathbf{r})$ has to be written as follows:

$$\psi = \sqrt{6\frac{\rho\left(\frac{RT}{1-b\rho} - a\rho - c_s^2\right)}{G}}. \quad (17)$$

Considering the linearized equation of state (6), the potential function is given by

$$\psi = \sqrt{\frac{6\left(\frac{\rho/\rho_0 - 1 + \alpha_p(T - T_0)}{\kappa_T} + p_0 - \rho c_s^2\right)}{G}}. \quad (18)$$

It has been pointed out [22] that, using this method, one can solve the Navier-Stokes equations

$$\partial_t\rho + \nabla\cdot(\rho\mathbf{u}) = 0,$$

$$\rho(\partial_t + \mathbf{u}\cdot\nabla)\mathbf{u} = -\nabla p + \nabla\cdot(\mu\nabla\mathbf{u}), \quad (19)$$

where the pressure is given by

$$p = \rho c_s^2 + \frac{G}{6}\psi^2, \quad (20)$$

and the kinematic viscosity is given by $\nu=\mu/\rho=(\tau-0.5)c_s^2\delta t$.

For treating buoyancy-driven flows the gravity force needs to be represented. This can be done by adding an external force term to the right-hand side of Eq. (11):

$$F_y = 3w_i g\alpha_p(T - T_{\mathrm{ref}})c_{iy}\delta t, \quad (21)$$

where T_{ref} is a reference temperature.

B. The energy equation

The energy equation is solved with a lattice Boltzmann model using another set of distribution functions. Since Eq. (3) is the well-known scalar transport equation for temperature with an extension of the work done by the compressibility, we basically extend the simple lattice Boltzmann model proposed by Inamuro *et al.* [25], taking into account the compression work.

So the following lattice Boltzmann equation is solved [details of the derivation of the macroscopic energy equation (3) from this mesoscopic equation is given in the Appendix]:

$$g_i(\mathbf{r}+c_{i\alpha}\delta t,t+\delta t)-g_i(\mathbf{r},t)=-\frac{1}{\phi}[g_i(\mathbf{r},t)-g_i^{\mathrm{eq}}(\mathbf{r},t)]+q_i, \tag{22}$$

in which the local equilibrium distribution function is defined as

$$g_i^{\mathrm{eq}}=w_i\left(T+\frac{c_{i\alpha}}{c_s^2}(Tu_\alpha-\tilde{D}_T\partial_\alpha T)\right). \tag{23}$$

The last term on the right-hand side of (22) is introduced to model the compression work and it is given by

$$q_i=-\delta t w_i\frac{RT}{c_v(1-b\rho)}\partial_\alpha u_\alpha \tag{24}$$

for the van der Waals gas, while it is written as

$$q_i=-\delta t w_i\frac{T}{c_v\rho}\frac{\alpha_p}{\kappa_T}\partial_\alpha u_\alpha \tag{25}$$

for the linearized equation of state.

Note that the equilibrium distribution function also has an extra term $\tilde{D}_T\partial_\alpha T$ when its current form is compared with the one proposed in [25]. This term assures that the heat diffusion can change in both space and time in our model.

The temperature is obtained as the first moment of the distribution functions:

$$T=\sum_i g_i. \tag{26}$$

In the numerical examples presented in the next section, the derivatives have been approximated by simple central difference schemes. It can be shown (see the Appendix) that the solution of the evolution equation (22) yields the solution of (3), and the transport coefficient is given by

$$\tilde{D}_{T,v}=D_{T,v}+(\phi-1/2)c_s^2\delta t. \tag{27}$$

C. Boundary conditions

For the numerical examples presented in the next section we had to model isothermal nonslip solid boundaries. These walls have been modeled by using the method proposed in [25,26]. Here the basic idea is to apply a counterslip velocity in the equilibrium distributions and determine the corresponding distribution functions, which step into the domain at the walls. For the diffusion and compression work terms the gradients have been evaluated by finite differences at the walls.

The evaluation of the gradient of the potential functions needs a slightly more elaborated approach. In our simulations the potential functions at the walls have been extrapolated from the potential of the inner nodes. That is, $\psi_{i,j+1}=2\psi_{i,j}-\psi_{i,j-1}$, where $(i,j+1)$ is a wall node, and (i,j), $(i,j-1)$ are in the fluid domain. Then (16) can be applied without modification just as at the inner nodes. The wettability of the walls has not been modeled.

IV. NUMERICAL SIMULATION OF HEAT TRANSFER

Three numerical examples are presented to demonstrate the applicability of our model. Our first numerical example is used to demonstrate that the proposed method can describe accurately heat transfer problems of fluids with variable heat conductivity, which is essential for supercritical fluids near the critical point. The second example demonstrates that the method can predict the heat transfer caused by the piston effect in a supercritical fluid near the critical point. In the third example we simulate the onset of convection in a Rayleigh-Bénard cell by considering a supercritical fluid.

A. Heat conduction with variable coefficient

We have simulated a fluid layer between two plates without gravity. The distance between the plates was unity. No-slip walls were used at the top and bottom boundaries and a periodic boundary condition was applied in the horizontal direction.

The thermal conductivity of the fluid depended on the temperature and it was given in the form

$$k=k_0(1+mT), \tag{28}$$

where m is an adjustable parameter.

The lower and upper plates had the temperatures T_l and T_u, respectively. In steady state the temperature is equilibrated between the plates by heat conduction and there is no flow in the domain. Accordingly, the Laplace equation can be solved, giving the analytical solution

$$T=\frac{\sqrt{(1+mT_l)^2+[(1+mT_u)^2-(1+mT_l)^2]y}-1}{m}. \tag{29}$$

Since the problem is actually one dimensional, the simulation domain had the size 4×50 lattice nodes. The relaxation times were $\tau=1$ and $\phi=0.8$. The temperatures at the lower and upper plates were 0 and 1, respectively. The variation of the heat conductivity was taken into account in the form of (28) by changing $D_{T,v}$ in each time step as follows: $D_{T,v}=\frac{\phi-1/2}{3}\delta t m T$.

In Fig. 3 the temperature profiles obtained from a simulation after equilibrating the temperature and calculated from Eq. (29) are shown for a parameter $m=10$. Obviously, the agreement is very good, demonstrating the proper treatment of the heat conductivity and the boundary conditions. In steady state the velocity was zero in the overall domain up to round-off errors.

B. Heat transfer enhancement due to the piston effect

As a second numerical example a fluid layer slightly above the critical point has been heated from below. The simulation domain was divided into 20×100 lattice sites and no-slip walls were used at the top and bottom boundaries. The periodic boundary condition was applied in the horizontal direction. The parameters of the van der Waals fluid were $a=9/8$, $b=1/3$, $R=1$ so the corresponding critical values are unity: $\rho_c=1$, $T_c=1$. The relaxation parameters were chosen to be $\tau=0.8$ and $\phi=0.7$.

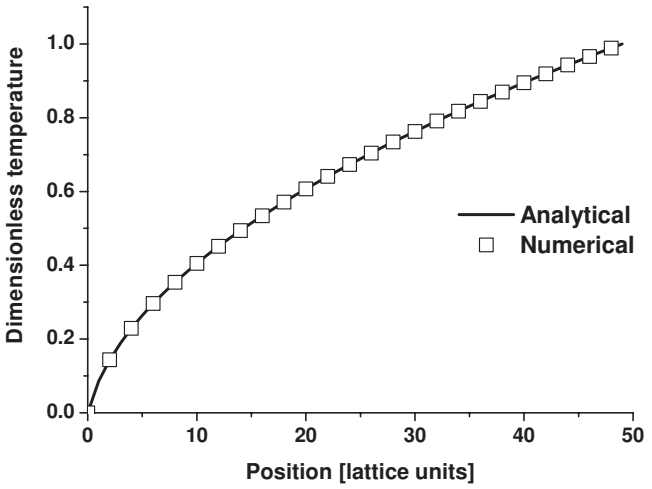

FIG. 3. Temperature profile as a function of position for a variable heat conduction problem.

Initially the fluid was at rest, $u_x=u_y=0$, and its initial temperature was above the critical point. Several simulations have been carried out with different initial temperatures and accordingly $\varepsilon=T-T_c$, but keeping the initial density as $\rho=1$ in the overall domain. Each simulation was started with a small temperature jump $\Delta T=0.003$ at the lower boundary. The temperature at the upper plate was kept constant. Similar simulations have been carried out in [14,3]. So we can give a qualitative comparison with those calculations.

In Fig. 4. the time evolution of the normalized temperature (T/T_{initial}) in the vertical center of the layer (top figure) and in the boundary layer at the bottom plate are shown for various initial temperatures. According to the diffusive scenario, the temperature at the center of the channel should start to increase smoothly only in some time after the temperature jump at the lower plate. Instead of this slow process, Fig. 4 shows that the heat transfer speeds up due to the piston effect in the case of a supercritical fluid. Almost immediately after the temperature jump, heat is transferred to the center because the thin boundary layer developed on the bottom starts to expand due to the high thermal expansion of the fluid. This expanding boundary layer, like a piston, compresses the rest of the highly compressible fluid and the compression heats the bulk up adiabatically. As a consequence of the expansion of the boundary layer, the density drops down rapidly in the boundary layer (see Fig. 4, bottom). Mass conservation implies that the expansion within the boundary layer is compensated by density increase in the bulk. Due to the piston effect the heat equilibration is very rapid and not smooth at all. Note that the amount of thermoacoustically transferred heat gradually decreases as we move further from the critical point by increasing the initial temperature. This is a consequence of the gradually decreasing compressibility and thermal expansion coefficient. At higher thermal expansions, the density drop in the boundary layer is more intense as would be expected.

In Fig. 5 a sequence of snapshots of the spatial temperature distributions in the channel is shown at various steps (step 100, 500, and 2000). The plots show the typical picture of temperature distributions observed in the numerical ex-

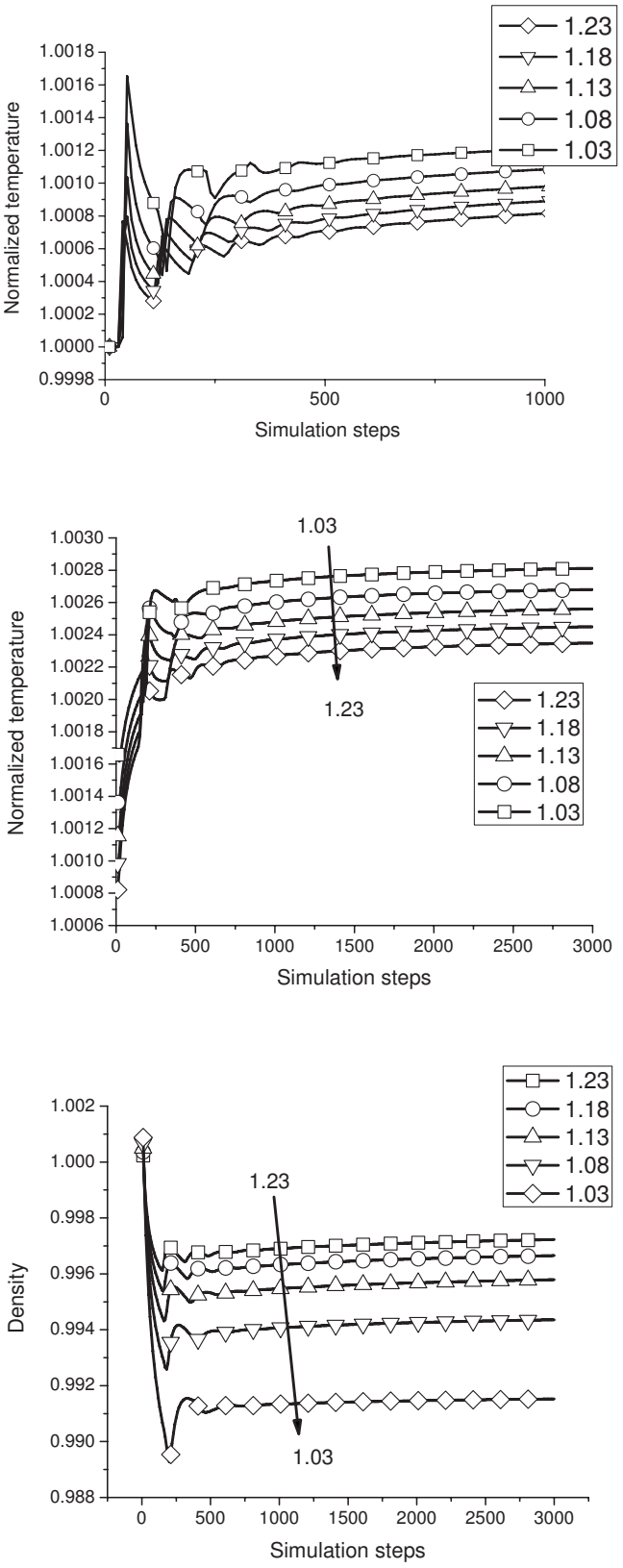

FIG. 4. Normalized temperature T/T_{initial} at the vertical center of the layer (top), temperature at the bottom boundary layer (middle), and the density at the bottom boundary (bottom) as a function of time after the temperature jump at the lower plate. The legend shows the initial temperature.

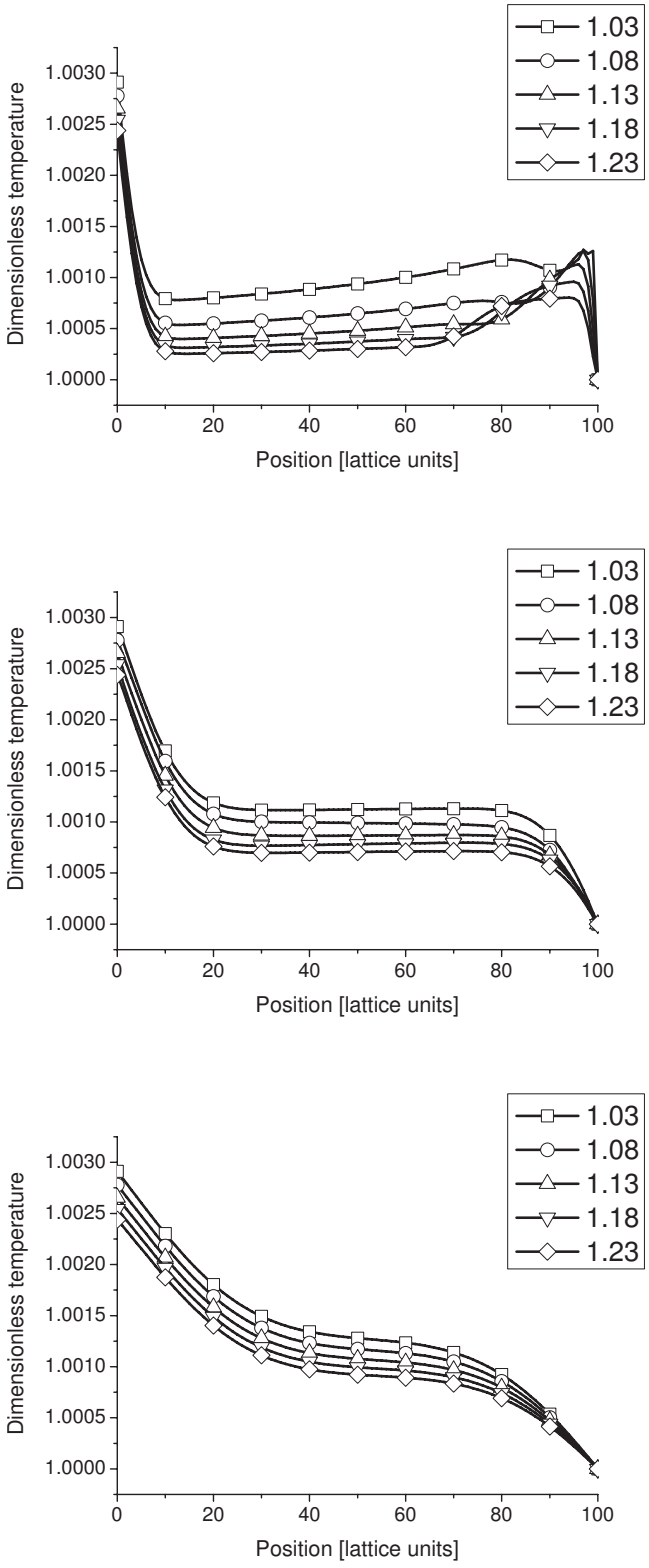

FIG. 5. Spatial distribution of the temperature in the layer at steps 100, 500, and 2000. The legend displays the applied temperature jump.

periments of other researchers (see, e.g., [14]). The temperature is homogeneously increased in the channel and the hot and cold thermal boundary layers can be observed clearly near the walls. Before 300 steps the distributions are not

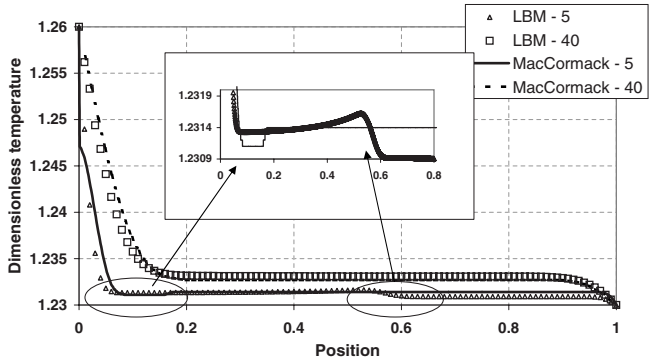

FIG. 6. Comparison of simulation results obtained by the lattice Boltzmann method and the MacCormack scheme.

fully homogeneous in the bulk. Such observations have been given in only a few reports (see e.g., [3]) since, as has already been mentioned, most numerical studies apply the acoustic filtering procedure, averaging over the spatial variation of the pressure waves and taking into account only the time variation of the pressure in a homogeneous manner throughout the channel. As we do not apply acoustic filtering, the propagation of pressure waves and the associated heat transport can be followed in both time and space. However, it is worth noting that in our approach the pressure waves propagate with the lattice speed of sound. So in order to adequately represent processes in the acoustic time scale, this velocity has to coincide with the sound speed of the fluid. If the sound speed and the viscosity of the fluid are known, the required time step and spatial resolution of the simulation can be estimated from the relations $\nu=(\tau-0.5)c_s^2\delta t$ and $\delta x=c_s\delta t$ [27]. As we approach the critical point the sound speed decreases; however, it still remains high enough unless ε is extremely small. So an adequate representation of the acoustics can be quite challenging unless the system size and the required simulation time are small. On the other hand, the piston effect time scale $t_{\mathrm{PE}}=L^2/[D_{T,p}(c_p/c_v-1)^2]$ (where $D_{T,p}=k/\rho c_p$ is the thermal diffusivity at constant pressure) is much larger than the acoustic time scale $t_a=L/c_s$, $t_{\mathrm{PE}}\gg t_a$, therefore a proper representation of processes in this time scale can be easily achieved by the proposed method, as can be seen in the last figures of the sequence in Fig. 5.

For quantitative evaluation, we also solved the Navier-Stokes and energy equations (without acoustic filtering) using the MacCormack scheme with flux-corrected transport [28]. The same numerical approach has been used by Nakano and Shiraishi [29] for the simulation of the piston effect. The physical parameters were chosen as specified before and the wall temperature was 1.23. For the MacCormack scheme 8000 cells were needed to obtain grid-independent solutions on a uniform grid. The time step required for numerical stability was 5×10^{-5}. Using the lattice Boltzmann method (LBM) with 1000 and 2000 nodes, we could get practically the same temperature profiles in the same dimensionless times; therefore simulations presented here were obtained using 1000 nodes. In Fig. 6 we show the temperature distributions in the fluid layer at dimensionless time 5 and 40 (which correspond to 5000 and 40 000 LBM time steps; and 100 000

and 800 000 steps in the MacCormack scheme). The simulation results are in good agreement with each other. Small deviations can be seen in the earlier stage of the simulations, which are due to the fact that in the LBM we do not resolve the acoustics properly. As has been mentioned, in the LBM pressure waves travel with the lattice speed of sound, while in the MacCormack scheme the pressure and corresponding temperature waves travel with the real speed of sound. This can be seen in the inset, where we show that the temperature waves are out of phase in the two schemes. However, the acoustic filtering assures that the average effect of the traveling and reflected pressure waves is represented well in the LBM and, as can be seen in the figure, the two schemes give practically the same results as the time increases.

C. Onset of convection in a Rayleigh-Bénard cell

The study of the onset of convection in a Rayleigh-Bénard cell is a classical problem of thermohydraulics. Consider a viscous fluid layer between two plates in gravity. The distance between the plates is L. The layer is heated at the lower plate T_L while the upper plate is maintained at a lower temperature $T_U=T_L-\Delta T$. As is well known, there is no convection in the cell when the temperature gradient ΔT is too small. When ΔT is increased, the system loses its stability and at the limit ΔT_{onset}, convection starts in the cell. Using nonslip walls at the top and bottom the convection is established at $\text{Ra}=\text{Ra}_c \simeq 1708$ in incompressible fluids, where the Rayleigh number Ra is defined as follows:

$$\text{Ra} = \frac{\alpha_p \Delta T g L^3}{\nu D_{T,v}}. \tag{30}$$

The mechanical stability of a compressible fluid layer is lost at higher Rayleigh numbers, based on theory [30–32]. This is due to a stabilizing mechanism called the adiabatic temperature gradient $G_{\text{AT}} \equiv \frac{g\rho}{\alpha_p}(\kappa_T - \kappa_S)$, where κ_S is the isentropic compressibility. Accordingly, near the critical point where the fluid is highly compressible, there is a crossover between the Rayleigh and Schwarzschild criteria and the onset happens at

$$\text{Ra}_{\text{corr}} > \text{Ra}_c \simeq 1708 \tag{31}$$

where

$$\text{Ra}_{\text{corr}} = \frac{g l^4 \alpha_p \rho_c c_p}{\nu D_{T,v}} \left(\frac{\delta T}{l} - \frac{g T \alpha_p}{c_p} \right). \tag{32}$$

l and δT are the hot boundary layer thickness and the associated temperature gradient, respectively.

Convection experiments on supercritical ^{3}He in a Rayleigh-Bénard cell has been reported in [31]. The cell was heated by a constant heat flux at the bottom wall and the top wall was kept at a constant temperature. The experimental setup of Kogan and Meyer supported the theoretical predictions. On the other hand, temperature oscillations above the convection onset were observed at the bottom wall of the cell in the experimental setup. The appearance of these oscillations was predicted later by numerical simulations too [10,33,12]. Based on their numerical experiments, Amiroudine and Zappoli gave an explanation for the heat transfer oscillations, appointing the piston effect as the responsible driving mechanism.

We have used our lattice Boltzmann model to predict the critical Rayleigh number near the critical point in a supercritical fluid. The simulation domain is a rectangular box with the size $(n_x=40, n_y=20)$. The relaxation parameters were chosen to be $\tau=0.8$ and $\phi=0.7$. Nonslip walls were used at the top and bottom boundaries. A periodic boundary condition was applied in the horizontal direction. As an initial condition we set the critical density $\rho=\rho_c=1$ and the convection-free equilibrium temperature profile was defined slightly above the critical point $T_c=1.0$. To excite the unstable modes an initial small perturbation in the form of a cosine wave was applied to the temperature field, i.e.,

$$T(x,y) = T_L - \frac{y}{n_y - 1}\Delta T + 10^{-3} \cos(\pi x / n_x), \tag{33}$$

where $T_L=T_U+\Delta T$ and $T_U=1.03$.

A number of simulations have been done using the linearized equation of state, which provides a way to vary α_p while keeping $\beta_T=1$ constant. The specific heat at constant volume has been chosen to be $c_v=100$. Using the thermodynamic relations

$$\kappa_T (c_p - c_v) = T \alpha_p^2 / \rho, \tag{34}$$

$$c_p (\kappa_T - \kappa_s) = T \alpha_p^2 / \rho, \tag{35}$$

the G_{AT} contribution can be rewritten as follows:

$$G_{\text{AT}} = \frac{g T \alpha_p}{c_v + T \alpha_p^2 / \rho \kappa_T}. \tag{36}$$

Therefore at small values of α_p (far from the critical point) the adiabatic temperature gradient is negligible, so we have to get back the critical Rayleigh number of the incompressible fluid. As we increase α_p, the adiabatic temperature gradient is increasing and the critical Rayleigh number has to increase too, since the other parameters are nearly constant.

The accurate critical Rayleigh number can be determined as follows. In an incompressible fluid the amplitude of the initial perturbation exponentially decays when ΔT is less than ΔT_{onset}. Above this limit the perturbation grows exponentially. So the critical Rayleigh number can be determined by varying ΔT and studying the evolution of the perturbation. By determining the rate of growth of the perturbation, one can accurately estimate the critical Rayleigh number as discussed in [34]. We could not follow this procedure strictly, since the exponentially growing phase was very limited at some high α_p. Therefore we first looked for the approximate value of ΔT_{onset} and then a few simulations were carried out around this ΔT value. Then the critical Rayleigh number was evaluated by simple linear interpolation of the Rayleigh number between the growing and decaying phases.

Figures 7–9 show the time evolution of the maximum vertical velocity for three different α_p values. As can be seen in Fig. 7 ($\alpha_p=1$) the critical Rayleigh number is between 1704 and 1716, and obviously it is very close to 1710. Even considering the two limiting values the error is less than 1%,

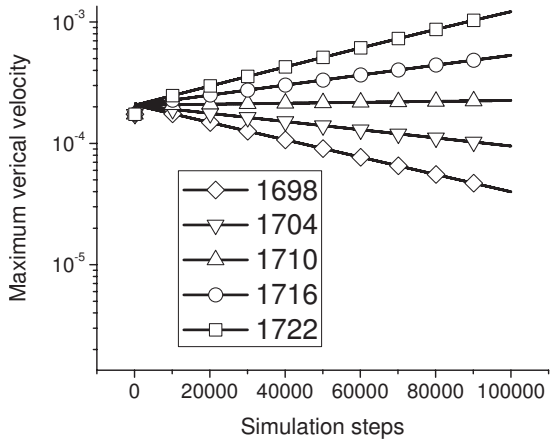

FIG. 7. Time evolution of the maximum vertical velocity at various Rayleigh numbers (α_p=1).

taking the theoretical value 1708 as a reference. In this computation the G_{AT} contribution is negligible.

As we approach the critical point (increasing the thermal expansion coefficient) the critical Rayleigh number gradually increases (Figs. 8 and 9). At α_p=5 the saturation of the velocity can be seen in the plot at the Rayleigh number 1962.

The overall picture of the simulations is given in Fig. 10 where the critical Rayleigh number as a function of $\alpha_p/\Delta T$ is shown. As expected, the critical Rayleigh number increases with α_p due to the stabilizing mechanism of the adiabatic temperature gradient. The increase of the critical Rayleigh number is a nearly linear function of $\alpha_p/\Delta T$, since the hot boundary layer and its thickness do not change significantly in the parameter range we studied.

V. CONCLUSION

We have proposed a lattice Boltzmann model for the numerical simulation of heat transfer in supercritical fluids. Numerical examples have demonstrated that the method can simulate heat transfer near the critical point, where several thermophysical parameters diverge. It has been shown that

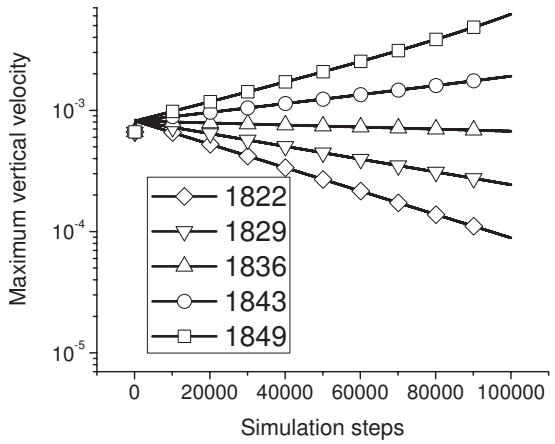

FIG. 8. Time evolution of the maximum vertical velocity at various Rayleigh numbers (α_p=3.75).

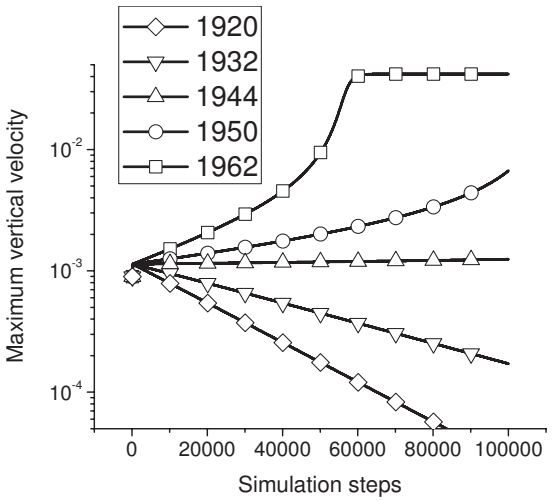

FIG. 9. Time evolution of the maximum vertical velocity at various Rayleigh numbers (α_p=5).

the critical speeding up of the heat transfer due to the rapidly increasing compressibility can be predicted by the proposed model. The onset of Rayleigh-Bénard convection has been studied near the critical point. The model can predict the critical Rayleigh number accurately far from the critical point. When the thermal expansion increased, the critical Rayleigh number increased in the simulations due to the stabilizing effect of the adiabatic temperature gradient, as was expected. Since the study of the crossover between the Rayleigh and Schwarzschild criteria is an intensive research field [8,9,11,35], we believe that the proposed model extended by a more realistic equation of state can be a useful tool in this research direction.

Although it has not been exploited in the current paper, we believe that our model can be especially useful when heat transfer on crossing the critical point needs to be studied. Below the critical point, a phase transition can take place, which is difficult to simulate by other numerical methods. On the contrary, the lattice Boltzmann method proposed here has been used mainly for phase transition problems before, so it might be a useful research tool for the modeling of such problems.

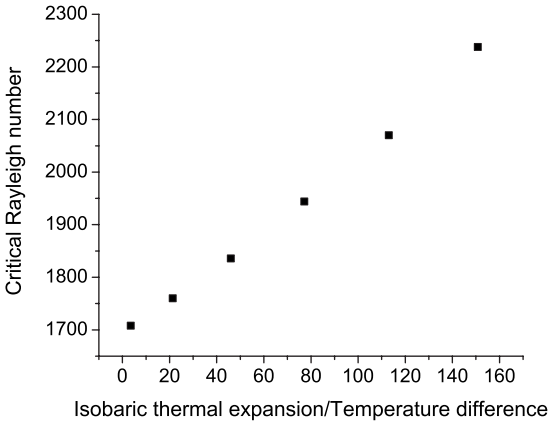

FIG. 10. Critical and corrected Rayleigh numbers as functions of α_p.

ACKNOWLEDGMENTS

This work was supported by the Hungarian Academy of Sciences in the framework of the NUKENERG project. The authors are grateful to Dr. Akihiro Nakano, National Institute of Advanced Industrial Science and Technology (AIST), Japan, for providing information on their simulation of the piston effect using the MacCormack scheme.

APPENDIX

Here we briefly review the derivation of the energy equation (3). The lattice Boltzmann equation for the energy is given as follows:

$$g_i(x + c_{i\alpha}\delta t, t + \delta t) - g_i(x,t) = -\frac{1}{\phi}[g_i(x,t) - g_i^{\mathrm{eq}}(x,t)] - \delta t w_i \frac{T}{\rho c_v}(\partial_T p)_\rho \partial_\alpha u_\alpha,$$

where the local equilibrium is

$$g_i^{\mathrm{eq}} = w_i\left(T + \frac{c_{i\alpha}}{c_s^2}(Tu_\alpha - D_{T,v}\partial_\alpha T)\right). \tag{A1}$$

Let us introduce the following series expansions:

$$g_i = g_i^{(0)} + \delta t g_i^{(1)} + \delta t^2 g_i^{(2)} + O(\delta t^3),$$

and the operator $D_i \equiv (\partial_t + c_{i\alpha}\partial_\alpha)$. Taylor expansion of the left-hand side of the lattice Boltzmann equation yields

$$\sum_{n=1}^{\infty} \frac{\delta t^n}{n!} D_i^n g_i(x,t) = -\frac{1}{\phi}[g_i(x,t) - g_i^{\mathrm{eq}}(x,t)] - \delta t w_i \frac{T}{\rho c_v}(\partial_T p)_\rho \partial_\alpha u_\alpha. \tag{A2}$$

Substitution of the expansions into (A2) and keeping terms up to second order gives

$$g_i^{\mathrm{eq}} - \phi\delta t D_t g_i^{(0)} - \phi\delta t^2 D_t g_i^{(1)} - \phi\frac{\delta t^2}{2} D_i^2 g_i^{(0)} - \phi\delta t w_i \frac{T}{\rho c_v}(\partial_T p)_\rho \partial_\alpha u_\alpha = g_i^{(0)} + \delta t g_i^{(1)} + \delta t^2 g_i^{(2)}.$$

Grouping terms according to their order in δt yields

$$g_i^{(0)} = g_i^{\mathrm{eq}(0)}, \quad O(\delta t^0),$$

$$g_i^{(1)} = -\phi D_t g_i^{(0)} - \phi w_i \frac{T}{\rho c_v}(\partial_T p)_\rho \partial_\alpha u_\alpha, \quad O(\delta t^1),$$

$$g_i^{(2)} = -\phi D_t g_i^{(1)} - \phi\frac{1}{2} D_i^2 g_i^{(0)}, \quad O(\delta t^2).$$

Substituting the first-order equation into the second-order equation, we obtain

$$g_i^{(2)} = -\phi\left(\frac{1}{2} - \phi\right) D_i^2 g_i^{(0)} + \phi^2 w_i D_t\left(\frac{T}{\rho c_v}(\partial_T p)_\rho \partial_\alpha u_\alpha\right).$$

It can be easily verified that $\Sigma_i(g_i - g_i^{\mathrm{eq}}) = 0$ and consequently $\Sigma_i(g_i^{(1)} + \delta t g_i^{(2)}) = O(\delta t^2)$, so

$$\sum_i (\partial_t + c_{i\alpha}\partial_\alpha) g_i^{(0)} + \sum_i w_i \frac{T}{\rho c_v}(\partial_T p)_\rho \partial_\alpha u_\alpha + \delta t \sum_i \left(\frac{1}{2} - \phi\right)(\partial_t^2 + 2\partial_t c_{i\alpha}\partial_\alpha + \partial_\alpha \partial_\beta c_{i\alpha} c_{i\beta}) g_i^{(0)} - \delta t \sum_i \phi w_i (\partial_t + c_{i\alpha}\partial_\alpha)\left(\frac{T}{\rho c_v}(\partial_T p)_\rho \partial_\alpha u_\alpha\right) = O(\delta t^2).$$

After some algebra we have

$$\partial_t T + \partial_\alpha(Tu_\alpha) - \delta t \phi \partial_t\left(\frac{T}{\rho c_v}(\partial_T p)_\rho \partial_\alpha u_\alpha\right) + \delta t\left(\frac{1}{2} - \phi\right)[\partial_t^2 T + 2\partial_t \partial_\alpha (Tu_\alpha - D_{T,v}\partial_\alpha T) + c_s^2 \partial_\alpha^2 T] = \partial_\alpha(D_{T,v}\partial_\alpha T) - \frac{T}{\rho c_v}(\partial_T p)_\rho \partial_\alpha u_\alpha + O(\delta t^2).$$

Using the fact that

$$\partial_t T + \partial_\alpha(Tu_\alpha) = \partial_\alpha(D_{T,v}\partial_\alpha T) - \frac{T}{\rho c_v}(\partial_T p)_\rho \partial_\alpha u_\alpha + O(\delta t),$$

we can simplify the equation above as follows:

$$\partial_t T + \partial_\alpha(Tu_\alpha) - \frac{\delta t}{2}\partial_t\left(\frac{T}{\rho c_v}(\partial_T p)_\rho \partial_\alpha u_\alpha\right) + \delta t\left(\frac{1}{2} - \phi\right)\partial_t \partial_\alpha (Tu_\alpha) = \partial_\alpha\left\{\left[D_{T,v} + \delta t c_s^2\left(\phi - \frac{1}{2}\right)\right]\partial_\alpha T\right\} - \frac{T}{\rho c_v}(\partial_T p)_\rho \partial_\alpha u_\alpha + O(\delta t^2).$$

Since the space derivatives are more dominant than the time derivatives, i.e., $\partial_t \sim \delta t \partial_\alpha$, we can consider the time derivatives, which have already had a multiplying factor δt as terms of $O(\delta t^2)$, so we can rewrite the equation above in the final form as follows:

$$\partial_t T + \partial_\alpha(Tu_\alpha) = \partial_\alpha\left\{\left[D_{T,v} + \delta t c_s^2\left(\phi - \frac{1}{2}\right)\right]\partial_\alpha T\right\} - \frac{T}{\rho c_v}(\partial_T p)_\rho \partial_\alpha u_\alpha + O(\delta t^2).$$

To increase the order of the method, an alternative solution has been recently proposed by Chopard and Latt [36], who canceled the undesired time derivative term by adding a counterterm to the lattice Boltzmann equation. Note that here we have assumed that ϕ is constant in space and time.

[1] F. Zhong and H. Meyer, Phys. Rev. E **51**, 3223 (1995).
[2] B. Zappoli, Phys. Fluids **4**, 1040 (1992).
[3] B. Zappoli, D. Bailly, Y. Garrabos, B. Le Neindre, P. Guenoun, and D. Beysens, Phys. Rev. A **41**, 2264 (1990).
[4] J. Straub, L. Eicher, and A. Haupt, Phys. Rev. E **51**, 5556 (1995).
[5] A. Onuki, H. Hao, and R. A. Ferrell, Phys. Rev. A **41**, 2256 (1990).
[6] H. Boukari, J. N. Shaumeyer, M. E. Briggs, and R. W. Gammon, Phys. Rev. A **41**, 2260 (1990).
[7] I. Pioro and R. Duffey, Nucl. Eng. Des. **235**, 2407 (2005).
[8] G. Accary and H. Meyer, Phys. Rev. E **74**, 046308 (2006).
[9] G. Accary, I. Raspo, P. Bontoux, and B. Zappoli, Phys. Rev. E **72**, 035301(R) (2005).
[10] S. Amiroudine and B. Zappoli, Phys. Rev. Lett. **90**, 105303 (2003).
[11] S. Amiroudine, P. Bontoux, P. Larroudé, B. Gilly, and B. Zappoli, J. Fluid Mech. **442**, 119 (2001).
[12] A. Furukawa, H. Meyer, and A. Onuki, Phys. Rev. E **71**, 067301 (2005).
[13] A. Furukawa and A. Onuki, Phys. Rev. E **66**, 016302 (2002).
[14] V. S. Nikolayev, A. Dejoan, Y. Garrabos, and D. Beysens, Phys. Rev. E **67**, 061202 (2003).
[15] S. Paolucci, Sandia Report No. SAND 82-8247, 1982 (unpublished).
[16] H. Swinney and D. Henry, Phys. Rev. A **8**, 2586 (1973).
[17] Data are taken from IAPWS-IF97, http://www.cheresources.com/iapwsif97.html
[18] A. Jounet, S. Amiroudine, A. Mojtabi, and B. Zappoli, Int. J. Thermophys. **19**, 1185 (1998).
[19] S. Succi, *The Lattice Boltzmann Equation for Fluid Dynamics and Beyond* (Clarendon Press, Oxford, 2001).
[20] S. Chen and G. Doolen, Annu. Rev. Fluid Mech. **30**, 329 (1998).
[21] M. Sukop and D. T. Thorn, Jr., *Lattice Boltzmann Modeling: An Introduction for Geoscientists and Engineers* (Springer-Verlag, Berlin, 2005).
[22] X. Shan and H. Chen, Phys. Rev. E **47**, 1815 (1993).
[23] P. Bhatnagar, E. Gross, and M. Krook, Phys. Rev. **94**, 511 (1954).
[24] H. Chen, S. Chen, and W. Matthaeus, Phys. Rev. A **45**, R5339 (1992).
[25] T. Inamuro, M. Yoshino, H. Inoue, R. Mizuno, and F. Ogino, J. Comput. Phys. **179**, 201 (2002).
[26] T. Inamuro, M. Yoshino, and F. Ogino, Phys. Fluids **7**, 2928 (1995).
[27] R. Nourgaliev, T. Dinh, T. Theofanous, and D. Joseph, Int. J. Multiphase Flow **29**, 117 (2003).
[28] C. A. J. Fletcher, *Computational Techniques for Fluid Dynamics 2* (Springer-Verlag, Berlin, 1988).
[29] A. Nakano and M. Shiraishi, Cryogenics **44**, 867 (2004).
[30] M. Gitterman, Rev. Mod. Phys. **50**, 85 (1978).
[31] A. B. Kogan and H. Meyer, Phys. Rev. E **63**, 056310 (2001).
[32] P. Carles and B. Ugurtas, Physica D **126**, 69 (1999).
[33] Y. Chiwata and A. Onuki, Phys. Rev. Lett. **87**, 144301 (2001).
[34] X. Shan, Phys. Rev. E **55**, 2780 (1997).
[35] G. Accary, I. Raspo, P. Bontoux, and B. Zappoli, Adv. Space Res. **36**, 11 (2005).
[36] B. Chopard and J. Latt, in Proceedings of the 16th Discrete Simulation of Fluid Dynamics Conference, DSFD2007, Banff, Canada, 2007 (unpublished).